



www.DeepakPublishing.com

Marinan, A. et al. (2018): JoSS, Vol. 7, No. 1, pp. 683–699
(Peer-reviewed article available at www.jossonline.com)



Analysis of the Microsized Microwave Atmospheric Satellite (MicroMAS) Communications Anomaly

Anne D. Marinan

*Jet Propulsion Laboratory, California Institute of Technology
Pasadena, California*

Ayesha G. Hein, Zachary T. Lee, Ashley K. Carlton, and Kerri L. Cahoy

*MIT Department of Aeronautics and Astronautics
Cambridge, Massachusetts*

Adam Milstein, Michael Shields, Michael DiLiberto,
and William J. Blackwell

*MIT Lincoln Laboratory
Lexington, Massachusetts*

Abstract

The Micro-sized Microwave Atmospheric Satellite (MicroMAS) is a dual-spinning 3U CubeSat equipped with a passive microwave spectrometer that operated nine channels near the 118.75-GHz oxygen absorption line. The focus of this first MicroMAS mission (hereafter, MicroMAS-1) was to observe convective thunderstorms, tropical cyclones, and hurricanes from a near-equatorial orbit. A small fleet of Micro-sized Microwave Atmospheric Satellites could yield high-resolution global temperature and water vapor profiles, as well as cloud microphysical and precipitation parameters.

MicroMAS-1 was delivered in March 2014 to the launch provider, and was deployed from the International Space Station in March 2015. Engineering data and sensor telemetry were successfully downlinked within the first few days of on-orbit operation, but an anomaly prevented the successful validation of the science instrument.

This paper discusses the data reconstruction process used to determine the spacecraft state and diagnose potential failure modes using combinations of simulations and engineering models of key components. After analyzing the potential failure modes on both the ground station and the spacecraft, results indicate that one of the solar panels may have not properly deployed, leading to the most likely cause of failure: damage to the onboard radio transmitter power amplifier. A re-flight mission, MicroMAS-2, has two launches (2a and 2b) planned for 2018.

1. Introduction

The term “nanosatellite” is applied to satellites that weigh less than 10 kg; a mass that is small enough to be easily accommodated as an auxiliary

payload on launch vehicles. A CubeSat is a standardized form of nanosatellite. The CubeSat specification document developed by the California Polytechnic State University in 2000 (California Polytechnic State University CubeSat Program, 2014) defines a

Corresponding Author: anne.d.marinan@jpl.nasa.gov

CubeSat unit, or a ‘U’ as the volume restriction of a cube with 10 cm on a side and mass of 1.33 kg per U. The widespread adoption of the CubeSat standard has resulted in a proliferation of commercial off-the-shelf (COTS) components suitable for use in space, including miniaturized power and communications systems, as well as miniaturized attitude determination and control systems that take advantage of advances in microelectromechanical systems (MEMS). The CubeSat units can be stacked or combined in a modular fashion, packed into single or multiple CubeSat deployers, and manifest on commercial or government launches to low Earth orbit. The National Aeronautics and Space Administration (NASA) maintains a CubeSat Launch Initiative (CSLI) program to increase launch availability to researchers.

A large majority of the several hundred CubeSat missions that have flown have experienced at least partial mission failure (Swartwout, 2016). The underlying causes vary, and can include attitude determination and control systems (Rowen et al., 2016), communication subsystems, power systems, or SD card failures (Springmann et al., 2012). There was even an instance of two CubeSats becoming unintentionally conjoined through the interaction of permanent magnets located on each of them that were intended to help stabilize attitude using the Earth’s magnetic field (Springmann et al., 2013).

Despite these failures, CubeSat capabilities are improving (NASA, 2014), and there is considerable momentum to transition from scientific and academic proof-of-concept missions into dedicated observation missions that generate valuable operational data products. MIT and MIT Lincoln Laboratory have collaborated on consecutive CubeSat efforts with the goal of advancing weather-sensing technologies. This paper focuses on the mission of the first Micro-sized Microwave Atmospheric Satellite (referred to herein as MicroMAS-1) (Blackwell et al., 2013), its operation, and the failure analysis that followed a loss of communication with the spacecraft early in the mission.

Section 2 gives an overview of the MicroMAS-1 mission and operations. Section 3 discusses the initial fault analysis and possible failure mechanisms considered when diagnosing a MicroMAS-1 communica-

tions anomaly. Section 4 presents the telemetry received and the methods used to determine an attitude solution and infer the state of other spacecraft subsystems. Section 5 analyzes the communication abilities of the satellite in two configurations, and Section 6 summarizes the findings of this paper.

2. The MicroMAS Mission and Operations

The Micro-sized Microwave Atmospheric Satellite (MicroMAS) seeks to observe convective thunderstorms, tropical cyclones, and hurricanes by using a spinning, passive microwave spectrometer with nine channels near the 118.75-GHz oxygen absorption line. The relatively low cost of CubeSat remote sensing facilitates the deployment of a constellation of sensors that could provide global revisit times approaching 40 minutes or better, a revolutionary step forward for atmospheric sounding and precipitation science (Marinan et al., 2013). MicroMAS-1 was the first flight of the miniaturized microwave instrument.

2.1. MicroMAS-1 Satellite Design

The 1U passive microwave radiometer payload was attached to a 2U supporting bus via a custom-designed scanner assembly (Peters et al., 2014). A twelve-channel slipring provided power and data connections between the bus and payload. The bus stack included a combination of COTS and custom-designed boards, as shown in Figure 1. COTS components in the board stack included an Electrical Power System (EPS) and 20 W-hr battery from Clyde Space, motherboard with PIC24 processor from Pumpkin, Inc., a UHF radio from L-3 Communications, and an integrated attitude determination and control system (ADCS) unit from Maryland Aerospace, Inc (MAI). The ADCS system included three-axis torque rods, three-axis reaction wheels, and two infrared Earth Horizon sensor assemblies. Custom designed electronics boards provided interfaces with the MAI unit, as well as the scanner assembly and payload.

MicroMAS-1 had a total of four deployable solar panel assemblies manufactured by Clyde Space, Inc. Each panel assembly consisted of a body-mounted

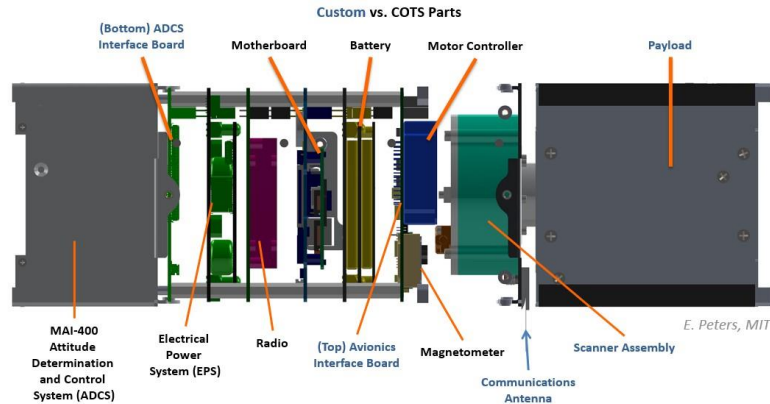


Figure 1. The MicroMAS-1 bus was composed of both custom and COTS components.

panel and a double-sided deployed panel for a total of twelve independent strings of solar cells. The panels were held in a stowed configuration with a tie-down mechanism. The deployed panels were connected to the body panels via hinges with torsional springs and secured with Dyneema cord. The deployment mechanism was a burn-through resistor. When commanded, current would flow through the resistors, and heat and melt the Dyneema cord, releasing the panel to deploy and lock at its intended deployment angle (120°).

The monopole antenna, which was connected to the L-3 Communications West Cadet UHF radio as the only method of on-orbit communication between the satellite and the ground station, was stowed underneath one of the deployed panels. Upon panel deployment, the tape-spring antenna was designed to automatically deploy.

2.2. MicroMAS-1 Ground Segment

The ground station for MicroMAS-1 was based on the infrastructure set up and successfully used on the Dynamic Ionospheric CubeSat Experiment (DICE) mission (Gunther, 2014). An 18.3-m antenna at NASA Wallops was the primary method of communication with the spacecraft, performing both transmit and receive functions. The MicroMAS-1 team sent commands and received and analyzed data packets via a network connection to the site at Wallops.

There was no GPS receiver on MicroMAS-1, so the location of the spacecraft was determined using

two-line elements (TLEs) provided by NORAD through the SpaceTrack or Celestrak services. The TLEs were input to the ground station antenna to orient and track the satellite during each overpass. The beam width of the Wallops UHF 18-m dish is 2.9 degrees. The projected full-width, half-max (FWHM) diameter of the uplink signal was about 20 km at the MicroMAS-1 orbit altitude of 400 km.

2.3. MicroMAS-1 On-Orbit Operations

MicroMAS-1 was delivered to the launch provider via NanoRacks in March 2014, and launched to the International Space Station (ISS) in July 2014. It was deployed from a NanoRacks deployer on the Japanese arm of the ISS (Figure 2) on March 4, 2015.

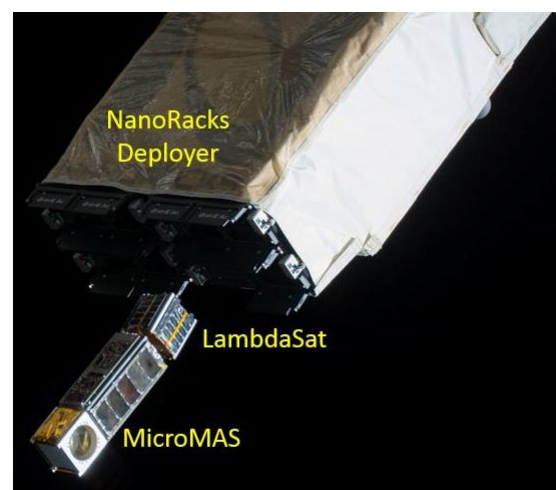


Figure 2. MicroMAS was deployed from the NanoRacks deployer on the ISS on March 4, 2015. Another satellite, the 1U CubeSat LambdaSat, was housed in the same deployer.

During each overpass, due to limitations of the radio, only a subset of the data queue was requested, and each data request involved a 30-second turnaround time to accommodate data demodulation in real time. Communication was established on the second overpass on March 4th, but there were only three total successful overpasses in which data were collected. After March 9, 2015, there were no successful downlinks, and in this paper, we assess the cause, which was suspected to be a spacecraft communications subsystem failure. Figure 3 shows a timeline of when each downlink occurred.

Most of the telemetry received was from ground testing (the radio queue was not cleared before launch) or when the spacecraft was in safe mode. The snapshots of spacecraft telemetry in safe mode contained power, temperature, IMU data, and the spacecraft status summary. There was one set of data that represented 2.5 minutes on orbit during which the ADCS unit was powered on, which enabled the collection of additional data from the Earth Horizon

Sensors, magnetometer, and coarse Sun sensors.

3. MicroMAS-1 Failure Assessment

3.1. Unlikely Failure Modes

There were four branches of a failure mode identified for the MicroMAS-1 mission, as shown in the “fishbone” diagram in Figure 4 below: Communications Operations, Space Vehicle, Ground Station, and Cadet Radio.

The ground station and communications operation branches were determined to be functioning as expected. Over-the-air tests with an engineering unit of the radio, as well as analyses of the link budget, verified the ground segments of Communications Operations and Ground Station branches. The ground station antenna pointing was ruled out by tracking the sun and pointing to spacecraft in similar orbits. The antenna was able to track all of those objects successfully. TLEs are frequently inaccurate, but we developed a method to assess the self-consistency of each



Figure 3. Timeline of spacecraft state during three successful overpasses.

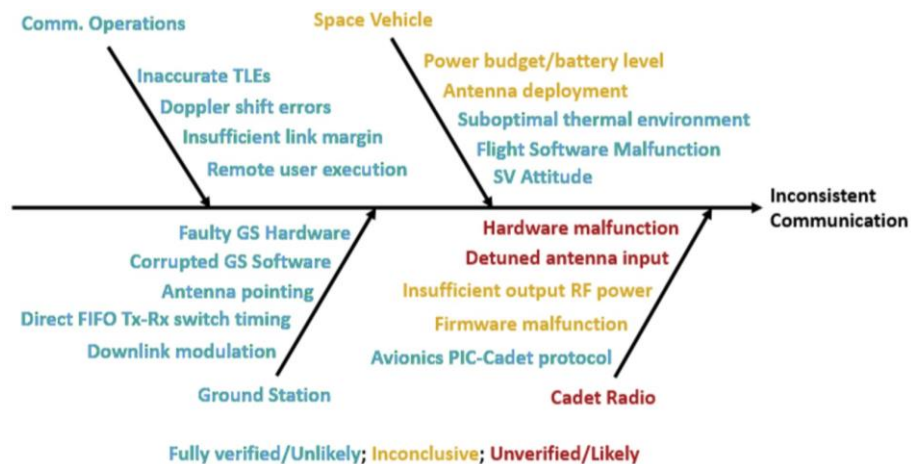


Figure 4. Four branches were identified to categorize possible causes for inconsistent communications with MicroMAS-1. The ground segments and some of the spacecraft state were ruled out early in operations, but radio and spacecraft states required more detailed analysis.

TLE and predict which passes would be less likely to fail from a position error perspective (Riesing, 2015). For the majority of the mission, the TLE error accuracy was expected to be well-within the 20-km antenna footprint.

Following these analyses, the space vehicle state and the spacecraft radio remained the main contenders for the anomaly behind inconsistent communications. After multiple command variations over several days, the team suspected that the spacecraft was successfully receiving commands, but was unable to transmit, and the most likely anomaly involved a transmitter failure.

3.2. Possible Spacecraft Failure Modes

The failure analysis performed early in the mission could not fully rule out hardware malfunction or de-tuned antenna input as possible causes of failure, as the power amplifier on the Cadet radio had failed before delivery during ground testing. The failure was observed when the radio was powered on with an unterminated SMA connection (which would normally connect to the antenna). Both the power amplifier and the processor on the motherboard were damaged during this incident as a result of reflected power ringing through one of the voltage lines. The radio board was reworked and the power amplifier was replaced prior to spacecraft delivery.

3.2.1. Hardware Malfunction

On-orbit data collected from MicroMAS-1 indicated that the spacecraft was receiving commands but

not transmitting properly. Telemetry captured via downlink on March 9 showed that during an overpass on the afternoon of March 5, the spacecraft had received commands to transmit, but all six of the transmission attempts were not received on the ground. Current telemetry indicated that the radio was not drawing the expected power from the raw battery line. Telemetry from a successfully down-linked signal is illustrated in Figure 5. Significant current draw on the raw (8 V) battery line is required

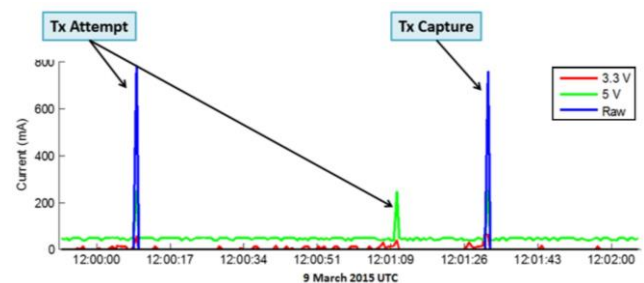


Figure 5. EPS data from a successful overpass shows the expected current draw during a nominal transmission.

for a successful transmission. The expected current draw on the raw battery line was absent from the power subsystem telemetry during unsuccessful transmission attempts (Figure 6). These data support the conclusion that the power amplifier was not operating nominally.

3.2.2. Antenna Failure

The other unverified fault scenario was de-tuned antenna input, which was related to the successful deployment of the antenna. While in the dispenser, the tape-spring antenna was stowed underneath a so-

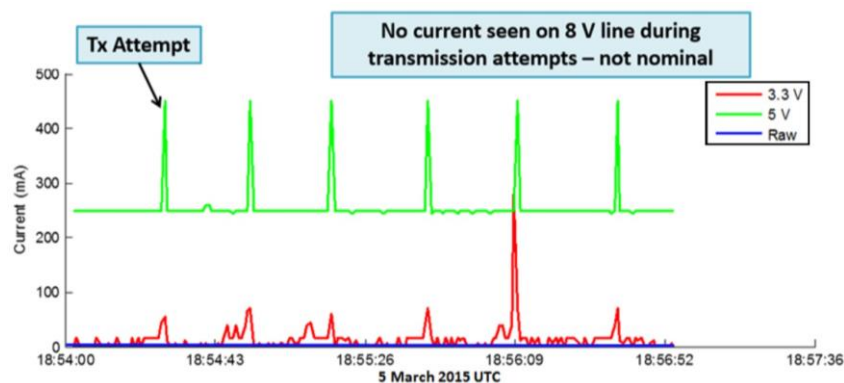


Figure 6. EPS data from an unsuccessful overpass show successful receipt of commands and indicate possible transmitter issues.

lar panel and held in place by a standoff inserted into an oval-shaped cutout in the tape-spring. The standoff prevented sideways motion from the stowed antenna that could scratch or damage the solar panel during transport and launch (see Figure 7). Upon panel deployment, the standoff was designed to slide out of the cutout and release the tape-spring to deploy.

During ground deployment testing, burrs on the solar panel standoff caused the antenna to become stuck and prevented the panel from fully deploying. Once discovered, the burrs were filed down and subsequent ground tests of the panel deployments were successful.

The antenna hold-down mechanism was also designed with the intent of keeping the tape-spring from folding beyond a safe radius of curvature. When integrated with the solar panel, the top panel compressed the tape-spring such that it may have exceeded that design constraint. The resulting stowed state of the antenna was not assessed to verify that deployment would still have been successful after a full year of stowage.

The reception of several successful data downlinks and on-orbit solar panel telemetry initially suggested that the panel and antenna had fully and successfully deployed, but detailed analysis of the attitude data from a 2.5-minute snapshot of the spacecraft state reopened the issue of whether or not the antenna had fully deployed. Unsuccessful antenna deployment in theory could still permit communications, but a partially deployed antenna could result in a bad load match, and ultimately have negative consequences on the radio operations, reflecting power back into the power amplifier and damaging the sys-

tem. Section 4 presents the analysis and data reconstruction of the relevant on-orbit telemetry to further investigate this possibility.

3.3. Space Environment

Space weather was also considered as a possible cause of failure. High energy particles can cause single event upsets and contribute to the total ionizing dose, impacting and potentially harming spacecraft electronics (Srouf and McGarrity, 1988). COTS components can be at a higher risk since they are not designed to be “rad-hard” due to resource constraints. Particle flux measurements from the Geostationary Operational Environmental Satellites (GOES) are used as a proxy for the environment around Earth (but it should be noted that conditions detected by GOES are in GEO and may not represent the true on-orbit environment of MicroMAS-1 in LEO). March 2015 included periods of high solar activity. On March 7, GOES detected an X-class solar flare, followed by a proton enhancement starting March 15 and geomagnetic activity leading to aurora on Earth (NOAA, 2017). While these “St. Patrick’s Day” storms were the strongest of solar cycle 24 at the time of the MicroMAS-1 mission current (a typically weak) solar cycle, the spacecraft was already exhibiting anomalous behavior, leaving high energy-radiation as an unlikely primary cause.

4. Data Reconstruction

On-orbit attitude telemetry was used to reconstruct the most likely spacecraft state to simulate nominal sensor readings. We assessed the most likely cause of failure by comparing the simulated sensor

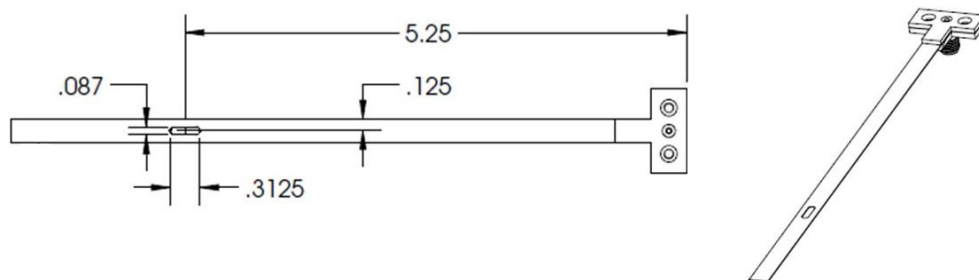


Figure 7. The tape-spring antenna featured an oval cutout through which a standoff on a deployable solar panel kept it in place when stowed. Dimensions are in inches.

readings to actual on-orbit values. The focus of this section is the generation of the attitude solution and analysis of the Earth horizon sensor readings and solar panel currents. The results indicate that one of the solar panels may have only partially deployed. The suspected panel (YN), the side-facing Earth horizon sensor, one of the coarse sun sensors (CSS), and the tape-spring antenna, as shown in Figure 8, were all located on the same side (Y+) of the spacecraft. We follow up this finding in Section 5 with an assessment of how the anomalous panel deployment likely led to the malfunction of the transmitter power amplifier that is believed to be the underlying cause of the communications anomaly.

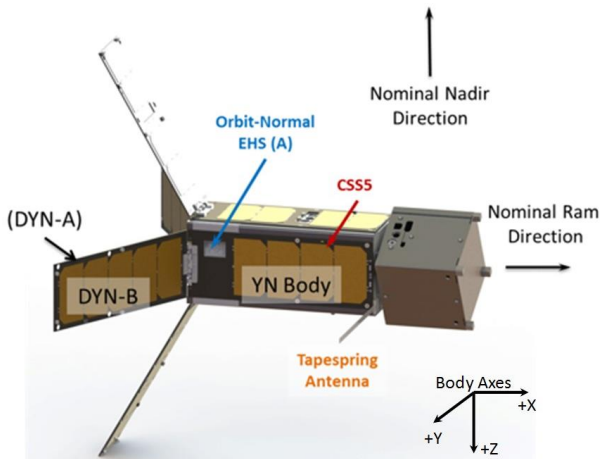


Figure 8. Rendering of MicroMAS-1 showing the coordinates and location of the antenna and EHS A on the same side as the YN Solar Panel.

4.1. Attitude Solution

The attitude sensors on MicroMAS-1 included a three-axis inertial measurement unit (IMU), three-axis magnetometer (MTM), six coarse sun sensors (CSS), and two earth horizon sensor assemblies (EHS). Each EHS assembly consisted of three fine and one coarse Earth Horizon Sensor, for a total of four sensors per assembly. The location and orientation of these sensors is illustrated in Figure 9. The flight attitude determination and control algorithms incorporate both TRIAD and extended Kalman filters (EKFs) to estimate and control the attitude (Wise, 2013; Quadrino, 2014).

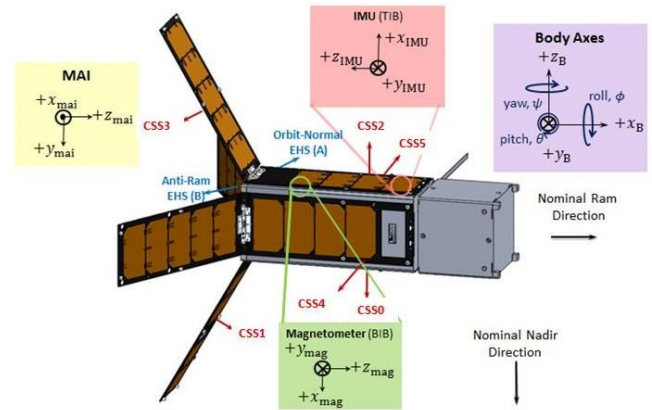


Figure 9. Locations and axes of attitude sensors on the MicroMAS-1 spacecraft. Note that the antenna, the EHS A sensor assembly, and CSS5 were located on the same side as the YN solar panel.

To determine an on-orbit attitude solution from the 2.5 minutes of retrieved attitude sensor telemetry, a Monte Carlo simulation was run with different attitude initializations using propagated gyro data resulting in a “best fit” smooth attitude profile for the coarse sun sensor measurements. The smooth attitude solution was then used to simulate a smoother, less noisy coarse sun sensor solution. Figure 10 compares the on-orbit telemetry with the model-generated sun sensor solution. The TRIAD algorithm was then run with the smooth CSS profile and satellite magnetometer readings to get a best-fit smooth attitude solution (Black, 1964). By design, that solution is consistent with the IMU, magnetometer, and (smoothed) CSS readings.

This solution can be used to reproduce the positions of the Sun “glints” and Earth “bumps” that are

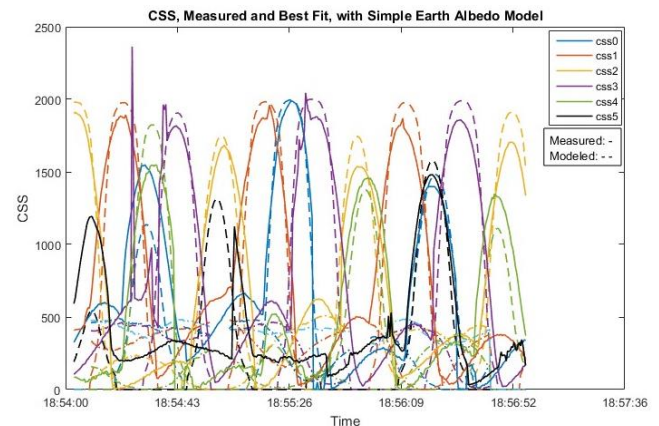


Figure 10. The smoothed sun sensor solution (dashed lines) matches all on-orbit CSS readings (solid lines) except CSS5 (black lines).

also seen in the EHS-B (anti-ram facing) data in Figure 11, giving some confidence that the attitude solution is reasonable.

There were also anomalous readings observed in the attitude sensor telemetry. The side-facing EHS assembly (EHS A assembly) located on the +Y side (this is the side with the YN panel) of the spacecraft saw readings that are too constant to be indicative of the likely spacecraft attitude. With the sun sensor-based attitude solution showing the spacecraft still tumbling, the likelihood of EHS A maintaining constant Earth-pointing throughout the period is very low. More likely, EHS-A is either obscured or malfunctioning. Additionally, the coarse sun sensor (CSS5), which is also located on the +Y side of the spacecraft, gave readings at a lower magnitude than the other five sun sensors. However, from this data alone, it cannot be ruled out that the hardware was simply malfunctioning. Section 4.3 analyzes the solar panel currents to further examine the possibility that the panel and antenna did not properly deploy.

4.2. Earth Horizon Sensor Analysis

Along with coarse Sun sensors, a magnetometer, and an inertial measurement unit, MicroMAS1 also employed two fixed assemblies of Earth horizon sensors (EHS) for attitude estimation, both of which

were present within the MAI-400 attitude determination and control system.

Infrared EHS are well-suited for use on CubeSats, because they are relatively inexpensive, small, and lightweight. Additionally, they can function both in sunlight and in eclipse. The EHS used for MicroMAS-1 were thermopiles that generated a voltage proportional to the net infrared heat flux. Each array of EHS included four thermopiles, all of which had Gaussian response curves. Three of the thermopiles had a conical 7° field-of-view and were considered to be narrow field-of-view (NFOV) sensors. The fourth thermopile had a conical field-of-view of 60° and was considered to be a wide field-of-view (WFOV) sensor (Maryland Aerospace Inc., 2014). The WFOV EHS was used for coarse attitude estimation. The NFOV sensors were used for fine attitude estimation, because their boresight vectors were such that when the spacecraft was in its nominal attitude configuration, one thermopile would receive little radiation from space, the middle one would have its field-of-view partially obscured by Earth, and one would receive radiation from Earth. By using two sets of EHS, a nadir vector can be calculated (Nguyen, 2014; Nguyen et al., 2017). For MicroMAS1, this nadir vector was sent into the TRIAD algorithm as one of the two reference vectors to estimate the satellite's attitude (Black, 1964).

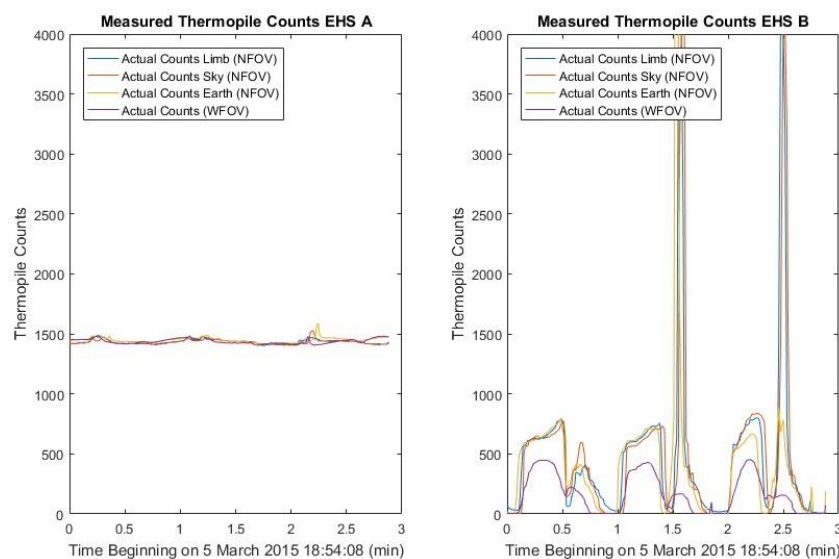


Figure 11. EHS telemetry, with EHS A facing in the +Y direction and EHS B facing in the -X direction.

The voltage generated by the thermopiles is proportional to the net infrared heat flux. The Stefan-Boltzmann law can be applied to give the heat transfer between two bodies, as shown in Equation 1 (Fortescue, 2011).

$$Q_{ij} = A_i F_{ij} \epsilon_{ij} \sigma (T_i^4 - T_j^4) \quad (1)$$

Q_{ij} is heat transfer, A_i is surface area, F_{ij} is view factor, ϵ_{ij} is emissivity, σ is the Stephan-Boltzmann constant, and T_i is the temperature. While Equation 1 describes the fundamental mechanism of radiation balance between two objects, it fails to account for the limited range of wavelengths that elicit a response and any physical characteristics of the sensor, such as a lens, that may affect the total radiation flux. Taking these into account, Equation 2 gives a more specific model for the voltage generated by thermopiles (Perkin Elmer Optoelectronics, 2001).

$$U_{tp} = SK(\epsilon_{target} T_{target}^4 - \epsilon_{target} T_{target}^4) \sin^2(\phi/2) \quad (2)$$

U_{tp} is the voltage generated by the thermopile, S is the sensitivity, K is the instrument factor, and ϕ is the cone angle for the thermopile. As shown in Fig-

ure 8, EHS A was on the side of MicroMAS-1 corresponding to the YN solar panels. EHS B was pointing in the antiram direction. Thus, EHS A was completely obscured by the YN panels before deployment, and if the YN panel only partially deployed, it would have blocked the field-of-view of the thermopiles. The measured counts from each of the thermopiles for the brief period for which sensor data is available is shown in Figure 11.

As shown in Figure 11, the measured response between EHS A and EHS B appeared different in that EHS A showed nearly consistent thermopile counts for the entire period, while EHS B showed values over the full range of the thermopile. Using the measured thermopile temperatures, the measured solar panel temperatures, and the relationships described in Equations 1 and 2, it was possible to estimate the expected EHS response if the sensors were obscured by the partial deployment of the YN panel. Because EHS B performed nominally and could not be obscured by any of the solar panels, this analysis was only conducted on EHS A. The measured EHS response and the expected response given full field-of-view saturation by the YN solar panel are shown in Figure 12. The equations used to generate these plots are based on Equations 1 and 2, but they also take into account the specific firmware and electronic

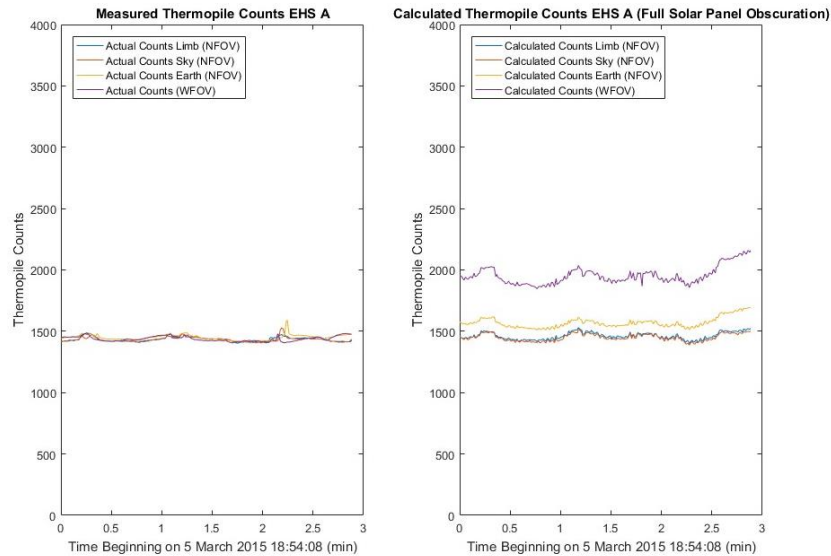


Figure 12. The measured thermopile counts for EHS A and the simulated counts that were calculated to correspond to the thermopiles' FOV being fully blocked by a partially deployed YN solar panel.

board components, which cause offsets and different scaling factors. The details of these equations are not shown, but the fundamental relationship between variables is as described in Equations 1 and 2.

While there is not perfect agreement, the number of thermopile counts predicted whether EHS A was viewing a solar panel instead of space and the Earth is reasonably close to the actual measured counts, especially given the potential range of 4000 counts. This seems to support the possibility of the solar panel only partially deploying. The WFOV sensor model results in a higher number of expected counts. This could imply that the WFOV sensor was only partly obscured by the solar panel and was partially viewing space, which would make the measured counts lower than the modeled counts.

The response of the WFOV sensors on both EHS A and B assemblies can also be compared with the expected values using the attitude solution described in Section 4.1. The expected response for operation vs. the actual response is shown in Figure 13.

The response of EHS B matches reality fairly well. The larger peaks shown align with the actual peaks, but the smaller ones are unaccounted for. This is likely due to the EHS responding to the Sun. With a 60° FOV, the WFOV EHS are more likely to see the Sun, although the NFOV also do seem to respond to the Sun, as seen in Figure 11 for EHS B, where the NFOV sensors appear to be fully saturated by the Sun. The curves for EHS A have no similarities, which implies that the sensor was malfunctioning or that the sensor FOV was filled by something other than the Earth, empty space, and the Sun.

Although the solar panel deployment of MicroMAS-1 was not fully observable, the EHS on-orbit data and subsequent ground analysis point towards a partial YN solar panel deployment such that the FOV of EHS A was nearly filled. The differences between the predicted response if seeing the partially-deployed solar panel and the actual telemetry can be attributed to several causes. First, the EHS FOV may have not been completely filled by the solar panel. If the FOV saw some of empty space or Earth, this would change the thermopile's response. Additionally, the solar panel may have not been in a static position, which would add noise to this effect. Last, model and attitude solution imperfections would cause disagreement. Despite some imperfections, there is much better agreement between the actual sensor data and the predicted response with a partially deployed YN solar panel than with one that is fully deployed.

4.3. Solar Panel Current Generation Analysis

Since it appears that the field of view of the EHS A assembly was filled by a solar panel, a more in-depth analysis of the power generation of each solar panel was of interest. The solar cells on MicroMAS-1 were Spectrolab Ultra Triple Junction cells with a 28.3% efficiency. Each body-mounted solar panel had four cells, while each deployed panel had five cells on each side, with the exception of the XN (nadir) panel, which had four cells on each deployed side to accommodate a cutout. The telemetry from each array showed that the panels on the YN side of the spacecraft had significantly different current generation patterns than that of the panels on the other

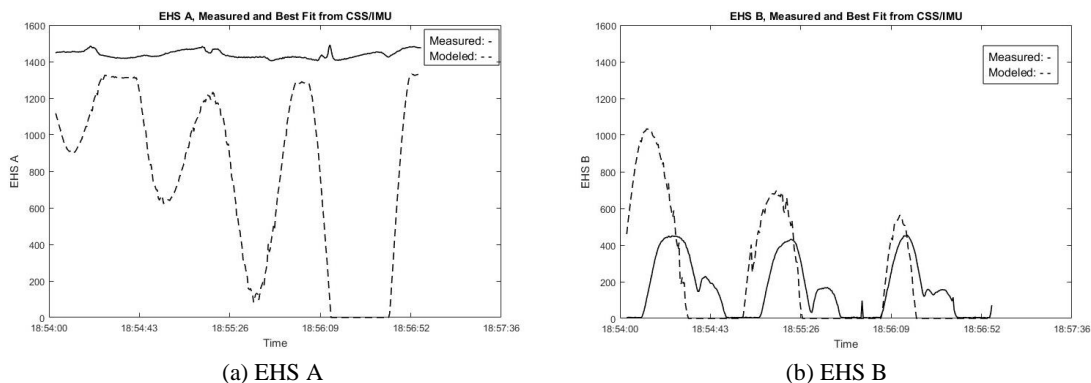


Figure 13. Expected Counts for Full Deployment (March 5, 2015; Times in UTC).

three sides. Figure 14 shows plots of the currents generated by the solar panels over the 2.5 min period of available telemetry.

From this telemetry, it appears that the magnitude of the current on the YN side along the body and Deployed-B panels was significantly less than the current in the same panels on the other sides of the spacecraft. This implies that the body and Deployed-B panels on the YN panels did not get as much solar input as the other panels. In the MicroMAS-1 stowed position, the body and Deployed-B panels were hidden (see Figure 8), suggesting that the deployable panel along the YN side may not have fully deployed.

To further investigate the anomaly in this telemetry, ground-based simulation of the currents in each solar panel was performed using the Systems Toolkit (STK) from Analytical Graphics, Inc. A model of the four deployed panels was created such that each deployed panel could be set to a range of deployment angles, and each string of solar cells was analyzed

independently. The attitude solution facilitated this detailed analysis of the solar panel current generation. The purpose of the analysis was to determine whether all panels deployed to their intended deployment angle of 120° . Figure 15 shows how the results from the model created in STK with all four panels deployed to their nominal deployment angle compare with the received telemetry.

These results show that the model captured the behavior of the telemetry data well for the XP, XN, and YP sides of the spacecraft. Each large peak in the telemetry corresponded to when each particular side faced the sun. Smaller peaks were attributed to the Earth's albedo. The sun and albedo peaks in the model line up with those in the telemetry. The magnitudes of each peak in the model also corresponded well with those in the model.

On the YN side, the model fit the telemetry poorly. The peaks in the telemetry did not line up with those from the model on the YN side. The model suggests that if the YN panel had deployed and

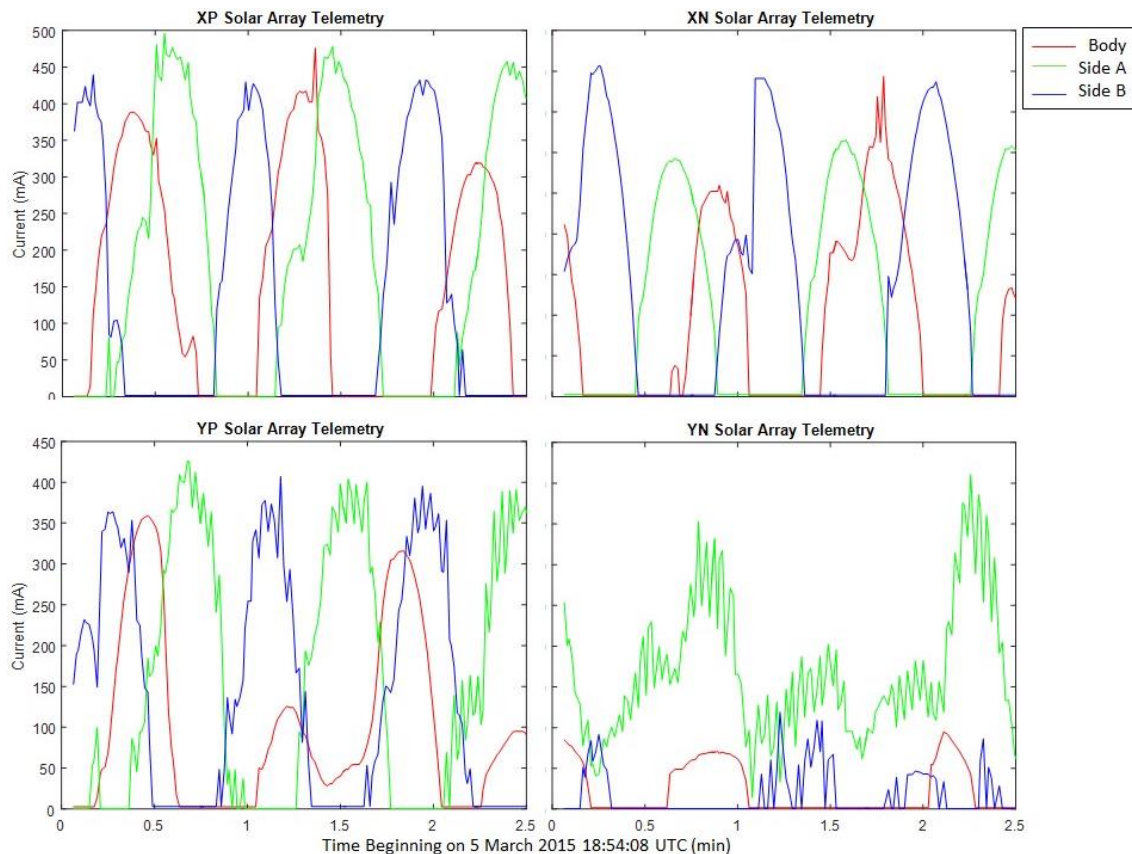


Figure 14. Telemetry of the solar panel strings showing an unexpected behavior in current telemetry from the YN side.

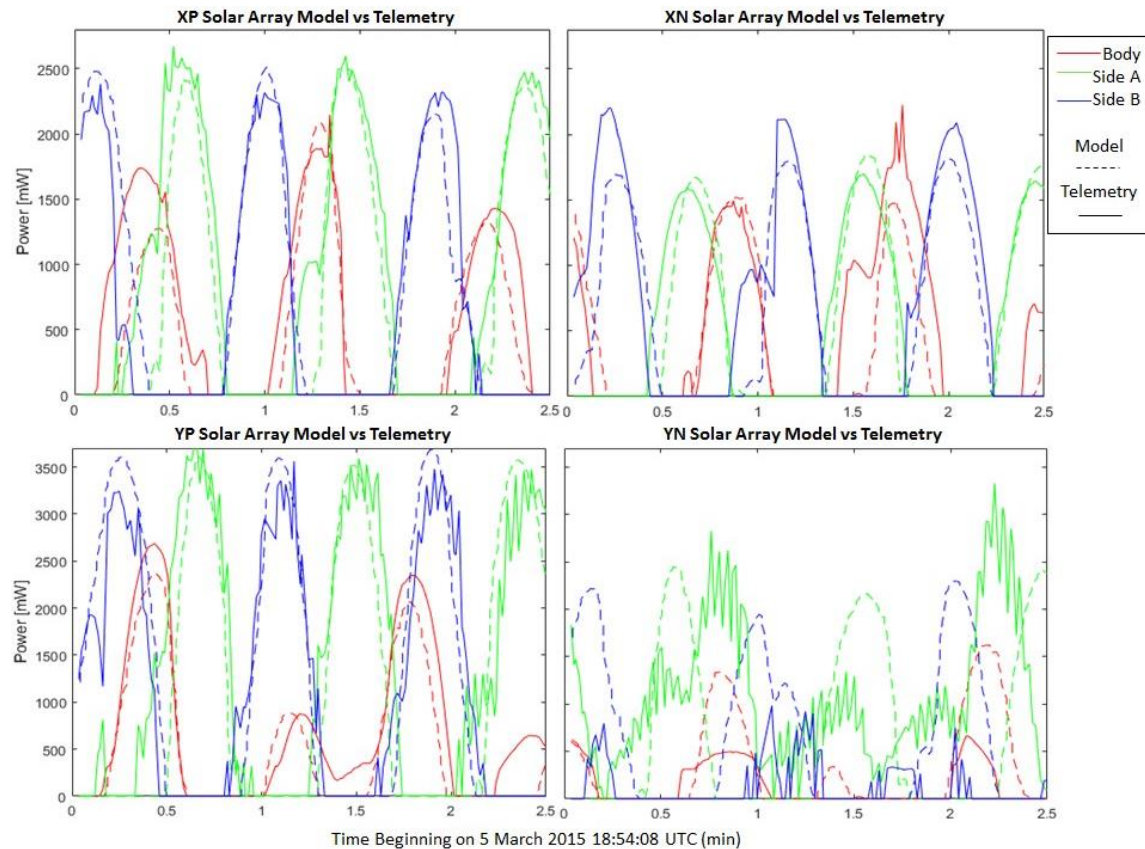


Figure 15. The solar array current telemetry (solid line) compared with model results (dashed line). The YN panel model, unlike the other three assemblies, does not match well with the on-orbit data.

worked properly, it would have had currents of the same magnitude as the currents in the other panels. The telemetry showed that this was not the case.

4.4. YN Solar Panel Deployment Angle Analysis

Because much of the data from sensors on the YN side of the spacecraft had unexpected values that suggest a panel deployment issue, the model of the spacecraft in STK was altered to analyze the possible angle of deployment of the solar panel. Figure 16 shows a model altered to have a panel partially deployed to 20° instead of the expected 120° of the other panels.

The STK current generation analysis was performed for different deployment angles of the YN panel ranging from 0° to 60° at 5° intervals. The model was used to generate solar array current telemetry in each of the three strings on the YN side. The results were compared to the telemetry received to

find the deployment angle which best fit the telemetry. Figure 17 shows the closest results with a deployment angle of 15°. From a geometric assessment using a model of the CubeSat, if the standoff on the solar panel and cutout in the tapespring antenna had prevented full panel deployment, as discussed in Section 3.2.2, the panel would not have been able to deploy beyond an angle of 18°.

Of the cases run, a deployment angle of 15° was the best fit of the model with the telemetry and showed significant improvement over the modeled telemetry from the YN panel if it had fully deployed (see Figure 15). The partial panel deployment model may not enable a perfect fit to telemetry, as it does not account for self-shadowing and possible cell defects. Limited by the 5° intervals, we estimate that the deployment angle of the YN panel was around 15°. This is consistent with the expected deployment if the antenna had prevented the panel from deploying properly.

panels due to the differences in absorptivity, emissiv-

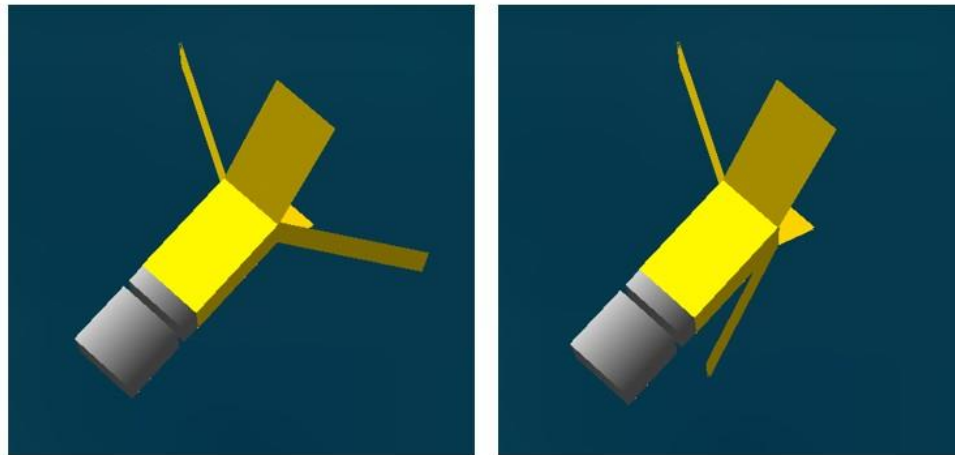


Figure 16. STK model of MicroMAS-1 with all panels deployed nominally (left) and as modified for a partially deployed YN panel (right).

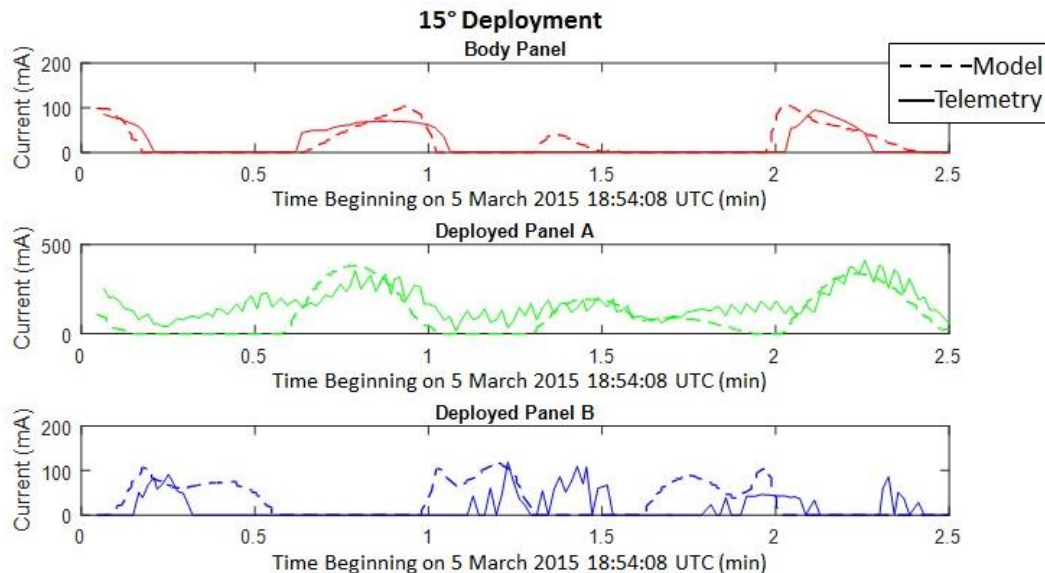


Figure 17. Modified STK model (dashed line) to include a partially deployed YN panel compared with YN panel telemetry (solid line).

4.5. Solar Panel Temperatures

The solar panel temperature telemetry further supports the theory of a partially deployed panel. Plots of the solar panel temperature telemetry are below in Figure 18.

The telemetry above shows that in all the panels except the YN panel, the difference between the temperature in the body panel and the deployed panel is about 25°C. We expect measurable differences in temperature behavior from the deployed and body

ity, and thermal paths between the body of the spacecraft and the deployed panels. However, for the YN panel, the difference between the temperature of the deployed panel and the body panel is only about 5°C. This could be explained by an off-nominal deployment angle. The closer the deployed panel is to the body panel, the closer the temperatures between the panels will be. This telemetry cannot be used to accurately estimate an angle of deployment, but does support the explanation of a partially deployed YN panel.

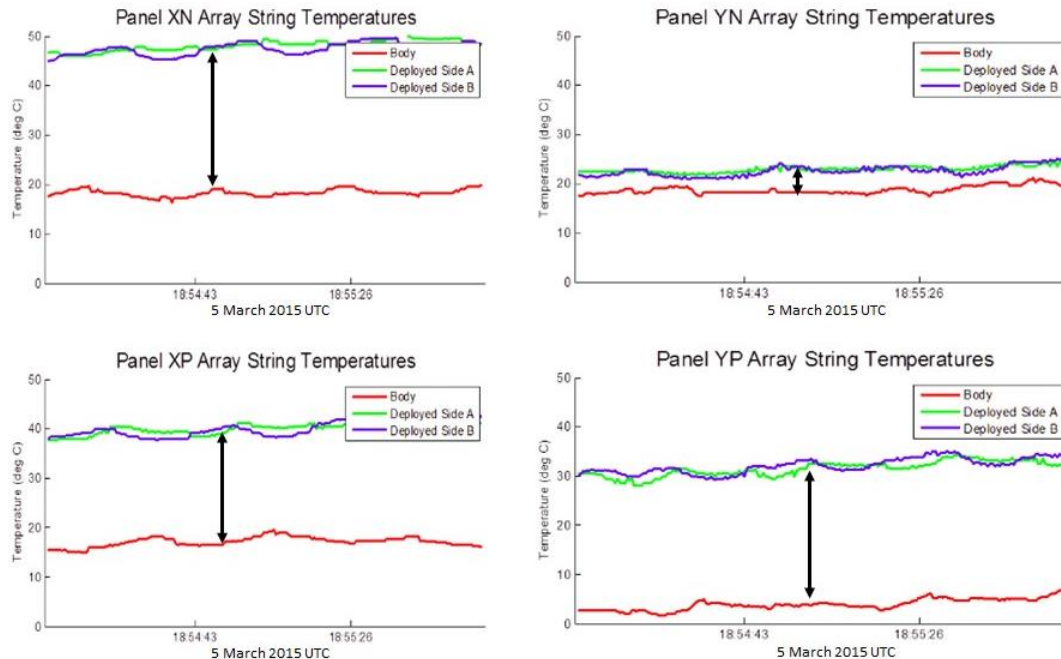


Figure 18. Solar panel temperature telemetry indicates a possible anomaly with the YN panel deployment, since the deployed panel temperatures are much closer to the body panel temperature than any of the other sides of the spacecraft.

5. Partial Deployment Communications Assessment

Post-failure, based on the evidence that the antenna panel may not have fully deployed, we ana-

lyzed what would have happened to the load match (reflected energy) at the antenna if it had not fully deployed, and considered the impact it may have had on the ability of the spacecraft to communicate. Figure 19 shows the two configurations tested.

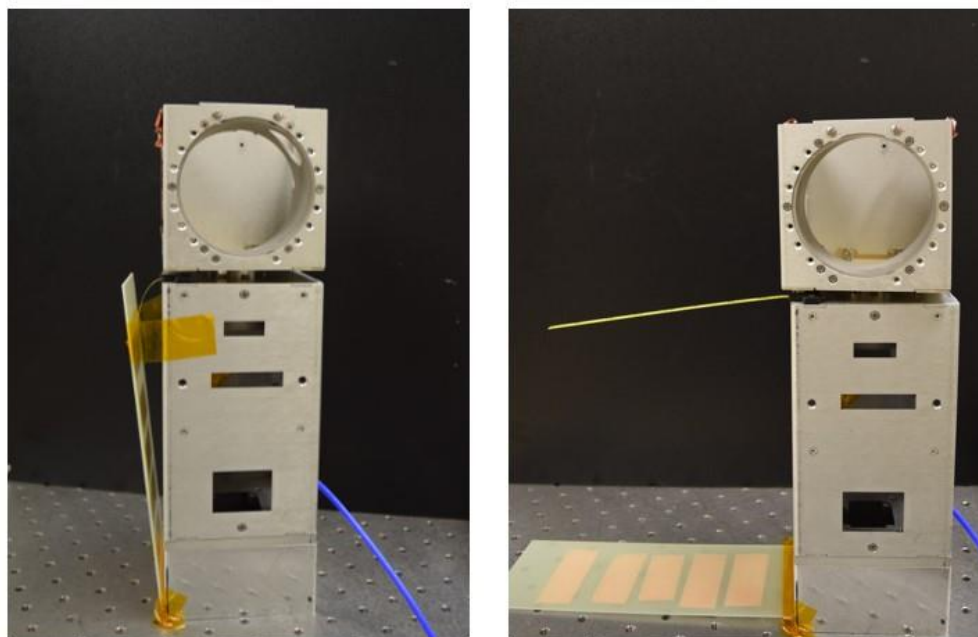


Figure 19. Left: MicroMAS mock-up in partially-deployed panel configuration. Right: MicroMAS mock-up in fully deployed configuration.

We measured the percentage of expected power that was transmitted and reflected by the antenna in each configuration: fully deployed, partially deployed, and partially deployed with copper tape as a stand-in model for the expected effect of the actual solar cells. Table 1 summarizes these results.

The MicroMAS link budget worst case analysis had a link margin of 0.4 dB at an elevation of 10°. This worst-case scenario included a several dB reduction in antenna gain, assuming a deployed antenna. The 85% reduction in transmit power from a partially-deployed antenna corresponds to an 8.24 dB loss. The best-case link budget assuming a deployed antenna had an additional 10–15 dB of margin. It is possible that the link could have been closed with a partially-deployed antenna, though the 85% reduction in transmit power does not include the additional gain lost due to the degradation of the antenna pattern that would result from the antenna being partially obscured by the panel. We did not expect to be able to close the link if the solar panel and antenna had not deployed at all.

While there was not a detailed simulation of the antenna pattern and loss due to panel obscuration, we note that the Cadet radio does not have any RF protection against reflected power, so it is likely that it would not take long for 85% reflected power to cause a transmit failure in the unit. Furthermore, one of the steps taken to try to establish more reliable communications with the spacecraft was to decrease the on-board attenuation from 6 dB to 0 dB. This was done before we had considered the likelihood of a partially deployed antenna, as it would have accelerated the damage to the radio.

6. Summary

This paper presents the on-orbit anomaly analysis for the MicroMAS mission in which inconsistent

(and eventually lost) communications ultimately prevented payload science validation. We used the few minutes of on-orbit attitude sensor data available to develop an attitude model, and used this model to compare sensor measurements to those expected during nominal operations to determine the most likely cause of failure.

The results of the failure assessment indicate that the likely cause of failure was the radio power amplifier, based on both the indications of inconsistent performance in the on-orbit EPS data during transmission attempts, and the likelihood that a partially deployed antenna resulted in a significant fraction of reflected power back at the transmitter. We recognize that there are several other potential sources of failure that cannot be completely ruled out.

Evidence from the sensor data and models support the theory that the YN solar panel assembly, which also constrained the tape-spring antenna, only partially deployed. The underlying cause was not fully verified, but speculation is that either the antenna cutout was caught on a standoff or the tape-spring was compressed to the point of failure while stowed for a year.

Using a spacecraft attitude solution based on the available on-orbit attitude data, we compared the expected EHS, solar panel currents, and solar panel temperatures with the measured values. We found that unusual behavior in the measured values on the YN side of the spacecraft could be explained by a partial panel deployment (around 15° instead of the intended 120°).

There were several lessons learned in operating and performing a failure analysis of MicroMAS-1. Subsequent missions have incorporated redundant communications systems and flight rules for verifying antenna deployment before commanding any high-power radio transmissions. Data from on-board sensors proved invaluable to assessing the most likely

Table 1. Summary of Results from Communications Test

Test Case	Return Loss (dB)	VSWR	% Transmitted	% Reflected
Fully Deployed	-13.59	1.09:1	0.9981	0.0019
Captured (with copper)	-0.71	12.3:1	0.15	0.85

spacecraft failure mode, though the detailed system simulation was not developed enough to use in operations until after the failure had occurred. While we did not have a full duplicate engineering model (EM) spacecraft, we did have an EM radio that allowed ground-based testing and verification of the ground station. Our ground station had high gain and a narrow beam-width, so orbit determination from a source besides TLEs (on-board GPS or two-way ranging) may have helped with communications earlier in the mission. Practicing ground operations was one of the most useful exercises for the team during the final integrated testing. More of that type of testing may have made early operations go more smoothly in terms of efficiency of commanding and data processing. Several tests and analyses that were done as part of the failure analysis would have been incredibly useful before the mission even launched.

As many CubeSat missions may attest, more support on high-level system oversight, a longer test campaign, or a full engineering model of the spacecraft may have led the team to identify and mitigate the observed failures earlier. That is not always a viable solution, given the cost, staffing, and schedule constraints of this and similar missions, so we strive for smarter design and testing based on these lessons learned.

Acknowledgments

This work was sponsored by the United States Air Force under Air Force contract FA872105-C-0002. Opinions, interpretations, conclusions, and recommendations are those of the authors and not necessarily endorsed by the United States Government. Additionally, the authors are grateful to the employees at Maryland Aerospace, Inc for their support in using the MAI-400. This work was supported by a NASA Space Technology Research Grant.

This work was done as a private venture, and not in the author's capacity as an employee of the Jet Propulsion Laboratory, California Institute of Technology.

References

- Black, H. (1964): A Passive System for Determining the Attitude of a Satellite, *AIAA J.*, Vol. 2, No. 7, pp. 1350–1351.
- Blackwell, J. et al. (2013): MicroMAS: First Step Towards a Nanosatellite Constellation for Global Storm Observation, in *Proc. AIAA/USU Conf. on Small Satellites, Technical Session XI: Around the Corner*, SSC13-XI-1. Available at: <http://digitalcommons.usu.edu/smallsat2013/all2013/120>.
- California Polytechnic State University CubeSat Program (2014): CubeSat Design Specification, Rev. 13. Available at: https://static1.squarespace.com/static/5418c831e4b0fa4ecac1bacd/t/56e9b62337013b6c063a655a/1458157095454/cds_rev13_final2.pdf (accessed April 29, 2018).
- Fortescue, P., Graham, S., and Stark, J. (2011): *Spacecraft Systems Engineering*, 4th ed., UK: John Wiley and Sons, Ltd.
- Gunther, J. (2014): Dynamic Ionosphere CubeSat Experiment High-Speed Satellite Ground Station. Available at: <https://www.ettus.com/application/detail/dynamic-ionosphere-cubesat-experiment-high-speedsatellite-ground-station> (accessed: April 29, 2018).
- Marinan, A., Nicholas, A., and Cahoy, K. (2013): Ad Hoc CubeSat Constellations Secondary Launch Coverage and Distribution, in *Proc. IEEE Aerospace Conf.*, p. 1–15. doi: 10.1109/AERO.2013.6497174.
- Maryland Aerospace Inc. (2014): MAI Static Earth Sensor [Factsheet]. Available at: <https://www.adcolem.ai.com/ir-earth-horizon-sensor> (accessed April 29, 2018).
- NASA Ames Research Center Mission Design Division (2014): Small Spacecraft Technology State of the Art, National Aeronautics and Space Administration. NASA/TP-2014-216648/Rev1, July 2014.
- NOAA National Geophysical Data Center (2017): Access to GOES SEM Data. Available at: <http://www.ngdc.noaa.gov/stp/satellite/goes/dataaccess.html> (accessed April 29, 2018).

- Nguyen, T. (2014): Attitude Determination using Infrared Earth Horizon Sensors, in *Proc. AIAA/USU Conf. on Small Satellites, Technical Session VIII: Frank J. Redd Student Competition*. Available at: <https://digitalcommons.usu.edu/smallsat/2014/FJRStudentComp/3/>.
- Nguyen, T., Cahoy, K., and Marinan, A. (2018): Attitude Determination for Small Satellites with Infrared Earth Horizon Sensors, accepted for publication in *AIAA J. of Spacecraft and Rockets*.
- Perkin Elmer Optoelectronics (2001): Remote Temperature Measurement with PerkinElmer Thermopile Sensors (Pyrometry): A Practical Guide to Quantitative Results. Available at: https://www.mantech.co.za/Technical/Attachments/TEMP_MEASUREMENT.PDF (accessed April 29, 2018).
- Peters, E. et al. (2014): Design and Functional Validation of a Mechanism for Dual-Spinning CubeSats, in *Proc. 42nd Aerospace Mechanisms Symposium*, NASA Goddard Space Flight Center, May 14–16, 2014.
- Quadrino, M. (2014): Testing the Attitude Determination and Control of a CubeSat with Hardware-in-the-Loop, SM Thesis, Dept. of Aeronautics and Astronautics, Massachusetts Institute of Technology, Cambridge, MA.
- Riesing, K. (2015): Orbit Determination from Two Line Element Sets of ISS-Deployed CubeSats, in *Proc. AIAA/USU Conf. on Small Satellites, Technical Session VIII: Student Competition*. Available at: <https://digitalcommons.usu.edu/smallsat/2015/all2015/58/>.
- Rowen, D. et al. (2016): OCSD-A / AeroCube-7: A Status Update, presented at the CubeSat Developers Workshop, San Luis-Obispo, CA, April 20–22.
- Springmann, J. C. et al. (2012): Development and Initial Operations of the RAX-2 CubeSat, in *Proc. 4S (Small Satellites Systems and Services) Symposium*, Portoroz, Slovenia, June 4–8.
- Springmann, J. C., Bertino-Reibstein, A., and Cutler, J. W. (2013): Investigation of the On-orbit Conjunction Between the MCubed and HRBE CubeSats, in *Proc. IEEE Aerospace Conf.*, pp. 1–8. doi: 10.1109/AERO.2013.6497127.
- Srour, J. R. and McGarrity, J. M. (1988): Radiation Effects on Microelectronics in Space, in *Proc. IEEE*, 76(11), pp. 1443–1469, 1988. doi: 10.1109/5.90114.
- Swartwout, M. (2016): CubeSat and Mission Success: A Look at the Numbers, presented at the CubeSat Developers Workshop, San Luis-Obispo, CA, April 20–22.
- Wise, E. (2013): Design, Analysis, and Testing of a Precision Guidance, Navigation, and Control System for a Dual-Spinning CubeSat, SM Thesis, Dept. of Aeronautics and Astronautics, Massachusetts Institute of Technology, Cambridge, MA.